Available online at www.sciencedirect.com
ScienceDirect
Trans. Nonferrous Met. Soc. China 33(2023) 3739−3755
Transactions of Nonferrous Metals Society of China
www.tnmsc.cn

# Microstructure and properties of Cu−Ni−Co−Si−Cr−Mg alloy by multistage thermomechanical treatment

Liu-xin QIN[1], Tao ZHOU[1], Xiao-yu JIANG[1], Meng WANG[1], Jin-hui HU[1], Zi-xiao WU[1], Xiang-peng MENG[1], Yan-bin JIANG[1,2], Zhou LI[1,2]

1. School of Materials Science and Engineering, Central South University, Changsha 410083, China;
2. State Key Laboratory of Powder Metallurgy, Central South University, Changsha 410083, China

Received 29 May 2022; accepted 30 August 2022

**Abstract:** A Cu−1.3Ni−1.2Co−0.7Si−0.3Cr−0.1Mg alloy with high strength and medium conductivity was designed and prepared. The effects of multistage thermomechanical treatment on the microstructure and properties of the alloy and its strengthening mechanism were studied. The results showed that a large number of nanoscale $\beta$-$Ni_3Si$, $\delta$-$(Ni,Co)_2Si$ and Cr phase particles precipitated in the high-density dislocation region and sub-grain boundaries during aging, and submicron $Cr_3Si$ phase particles formed during solidification of the alloy. The tensile strength, yield strength and electrical conductivity of the alloy were 882 MPa, 857 MPa and 46.7% (IACS), respectively. The main strengthening mechanisms of the alloy were precipitation strengthening, strain strengthening and sub-structure strengthening through the strengthening model calculation and measured strength.

**Key words:** multicomponent alloying; microstructure evolution; precipitated phase; properties; strengthening mechanism

## 1 Introduction

Cu−Ni−Si alloys have a wide application prospects in aerospace, transportation tracks, electronic information and other fields because they combine high strength, high elasticity and excellent electrical conductivity, thermal conductivity, and stress relaxation resistance [1−4]. The Cu−Ni−Si alloy represented by C70250 has a strength of 600−800 MPa and an electrical conductivity of 30%−40% (IACS) [5,6], which is mainly used in elastic components, integrated circuit lead frames and patch electronic devices [7−9]. With the development of electronic information and other high-tech industries, increasing requirements for the strength and electrical conductivity of copper alloys have been proposed [10,11]. It is difficult to meet the requirements of the existing Cu−Ni−Si alloys.

Cu−Ni−Si alloy is a kind of precipitation strengthening copper alloy, and its strengthening phases are mainly $Ni_2Si$ and $Ni_3Si$ phases [12,13]. Addition of Co can hinder spinodal decomposition and $DO_{22}$ ordering in the Cu−Ni−Si alloy during phase transformation [14]. XIAO et al [15] found that Co atoms in Cu−Ni−Co−Si alloy nucleate preferentially in the vacancy at the initial stage of aging, which is beneficial to reducing the content of Si in the Cu matrix and restrain the slip of movable dislocations. MONZEN and WATANABE [16] found that Mg element can accelerate the nucleation rate of the precipitates. Furthermore, the large difference of atomic radius between Mg and Cu elements helps to increase the recrystallization temperature of the alloy and improve its high-temperature softening resistance [17]. WANG et al [18] indicated

**Corresponding author:** Yan-bin JIANG, Tel: +86-13466312126, E-mail: jiangyanbin@tsinghua.org.cn
DOI: 10.1016/S1003-6326(23)66367-8

that adding Cr element can significantly refine the microstructure of Cu−Ni−Si alloys, and Cr phase and stable $Cr_3Si$ phase particles formed. Therefore, appropriate amounts of Co, Cr and Mg elements are added to the Cu−Ni−Si alloy. These alloying elements are dissolved in the matrix and precipitated in the form of different nanoscale second phases through subsequent multistage thermomechanical treatment to realize precipitation strengthening. Meanwhile, after the precipitation of solid solution elements, the electron scattering of copper matrix is weakened, and good electrical conductivity is achieved on the basis of greatly improving the strength of alloy, so as to play the synergistic effect of multicomponent alloying.

Heat treatment is an effective mean to improve the strength and electrical conductivity of copper alloy [19]. DONG et al [20] found that excessive deformation not only decreases the electrical conductivity but also causes the alloy to over-aging state. ZHAO et al [21] thought that after cold deformation of a supersaturated Cu−Ni−Si alloy, interaction between the phase transformation of precipitation and the Cu matrix recrystallization occurs during aging. Fine precipitates can hinder recrystallization, while the coarsening precipitation phase promotes recrystallization. LEI et al [22] indicated that with increasing deformation, dislocation loops near the precipitated phase gradually accumulate, resulting in an increase in the dislocation density near the precipitated phase, which easily induces the nucleation of the precipitated phase in the high-density dislocation. Through repeated cold rolling and aging, dislocations and sub-grains increase in the matrix and more nucleation sites are provided for the second phase particles. On the one hand, it is helpful to promoting the fully dispersed precipitation of the second phases, making the forming second phases effectively pin up dislocations and hindering grain boundary migration to improve the strength and electrical conductivity of the copper alloy. On the other hand, due to the poor precipitation kinetics of Ni, Co, Si, Cr and other elements, they cannot be precipitated in large quantities during one-time aging. Therefore, multistage thermomechanical treatment was used.

In this work, Cu−1.3Ni−1.2Co−0.7Si−0.3Cr−0.1Mg alloy with high strength and medium conductivity was designed and prepared by the synergistic effects of multicomponent alloying and thermomechanical treatment. The effects of different heat treatments on the microstructure and properties were studied. The precipitation behavior of the strengthening phases and the strengthening mechanisms during multistage thermomechanical treatment were revealed, which provided a guidance for the optimization of composition and synergistic improvement of properties on high strength and medium electrical conductivity of Cu−Ni−Co−Si alloys.

## 2 Experimental

Cu−1.3wt.%Ni−1.2wt.%Co−0.7wt.%Si−0.3wt.%Cr−0.1wt.%Mg alloy (hereinafter referred to as Cu−1.3Ni−1.2Co−0.7Si−0.3Cr−0.1Mg) ingot with sizes of 45 mm × 90 mm × 100 mm was prepared by medium frequency induction furnace using electrolytic copper (99.95 wt.%), pure nickel (99.95 wt.%), pure cobalt (99.95 wt.%), pure chromium (99.95 wt.%), Cu−30wt.%Si master alloy, and Cu−20wt.%Mg master alloy as raw materials. The melting temperature was 1250 °C, the casting temperature was 1150 °C, and the casting method was iron mold casting. The chemical composition of the alloy was measured by inductively coupled plasma atomic emission spectrometry (ICP-AES), and the results are listed in Table 1. The ingot was homogenized at 950 °C for 4 h and then hot rolled to a strip with a thickness of 8 mm, the hot rolling temperature was 920 °C, and the deformation was 80%. The hot rolled strip was solid-solution treated at 940 °C for 1.5 h and then quenched by water cooling. The strip after solid-solution treatment was subjected to multistage thermomechanical treatment, and the treatment parameters are shown in Fig. 1 and Table 2.

**Table 1** Chemical composition of Cu−1.3Ni−1.2Co−0.7Si−0.3Cr−0.1Mg alloy (wt.%)

| Element | Design composition | ICP-AES |
|---|---|---|
| Cu | 96.4 | Bal. |
| Ni | 1.3 | 1.29 |
| Co | 1.2 | 1.18 |
| Si | 0.7 | 0.66 |
| Cr | 0.3 | 0.26 |
| Mg | 0.1 | 0.1 |

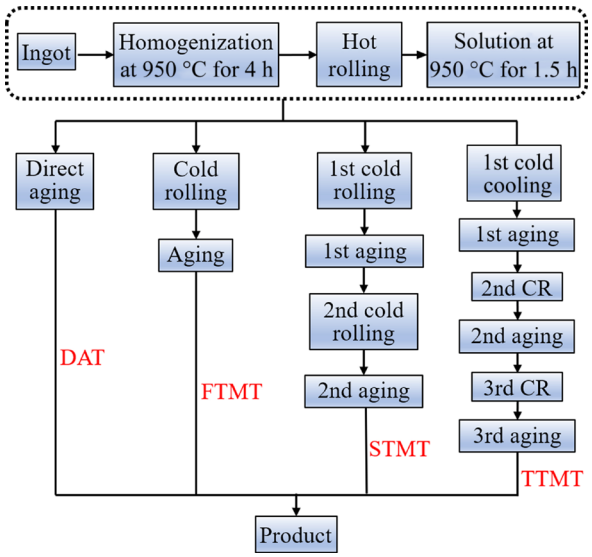


**Fig. 1** Technical route diagram

Tensile tests were carried out by an MTS material test machine at room temperature, with a constant velocity of 1 mm/min. Three samples of each condition were tested and the average value of the properties was taken as the test result. The hardness of the alloy was tested by an HV5 micro-hardness tester with a load of 1 kg and a holding time of 15 s. Five points of each sample were measured, and the average value of the properties was taken as the test result. Samples with sizes of 50 mm × 3 mm were cut from the alloy, and the resistance of the alloy was measured by a QJ36s DC resistance tester. Three samples of each condition were tested, and the electrical conductivity was taken and calculated from the average value.

For the transmission electron microscope (TEM) samples, the disk with a diameter of 3 mm and thickness of 120 μm was cut and then milled to 50−70 μm. The TEM samples were prepared by a RL-4 electrolytic instrument with a voltage of 10 V at −35 °C. The microstructures of the samples were observed by a Titan G2 60−300 TEM equipment.

## 3 Results

### 3.1 Mechanical and electrical properties of Cu−1.3Ni−1.2Co−0.7Si−0.3Cr−0.1Mg alloy

3.1.1 Effect of DAT on properties of alloy

Figures 2(a) and (b) show the hardness and electrical conductivity change curves of the Cu−1.3Ni−1.2Co−0.7Si−0.3Cr−0.1Mg alloy with aging

**Table 2** Multistage thermomechanical treatment processes for studied alloy

| Heat treatment | Process |
|---|---|
| Direct aging treatment (DAT) | Solution treated + aged at 400/450/500 °C for different time (0−480 min) |
| First-stage thermomechanical treatment (FTMT) | Solution treated + cold rolled by 60% + aged at 400/450/500 °C for different time (0−480 min) |
| Second-stage thermomechanical treatment (STMT) | Solution treated + cold rolled by 60% + aged at 450 °C for 1.5 h + cold rolled by 70% + aged at 350/400/450 °C for different time (0−240 min) |
| Third-stage thermomechanical treatment (TTMT) | Solution treated + cold rolled by 60% + aged at 450 °C for 1.5 h + cold rolled by 70% + aged at 350 °C for 0.5 h + cold rolled by 30% + aged at 300 and 350 °C for different time (0−480 min) |

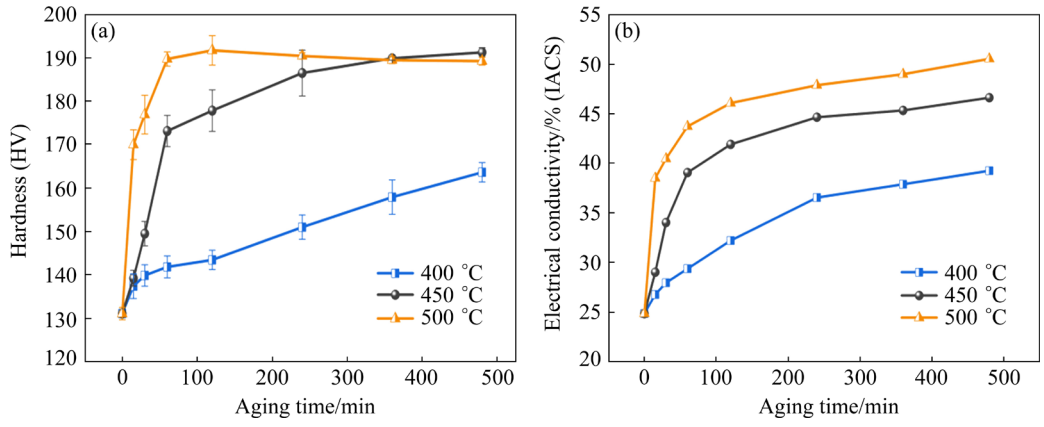


**Fig. 2** Variations of hardness (a) and electrical conductivity (b) of DAT samples

time at 400, 450 and 500 °C, respectively. The hardness and electrical conductivity increased with aging time, and the higher the temperature was, the shorter the aging time to reach the aging peak value. Taking aging at 500 °C as an example, when the aging time was 120 min, the hardness of the alloy reached the peak value and increased rapidly from HV 131 of the solid solution state to HV 192. When the aging time was prolonged, the hardness of the alloy decreased. For the cases of aging at 400, 450 and 500 °C for 480 min, the hardness was HV 163, HV 191 and HV 189, respectively, and the electrical conductivity increased from 25% (IACS) of the solid solution state to 39%, 46% and 50% (IACS), respectively.

3.1.2 Effect of FTMT on properties of alloy

The alloy was treated by the FTMT process (solution → 60% cold rolled → aged). Figures 3(a) and (b) are the hardness and electrical conductivity change curves of the FTMT samples with aging time, respectively. For aging at 400, 450 and 500 °C, the hardness and electrical conductivity increased rapidly with the extension of aging time to 30 min. With further prolonging the aging time, the hardness curves aged at 500 °C decreased significantly, while the hardness of the alloy aged at 400 and 450 °C increased slowly. Taking aging at 450 °C as an example, when the aging time was 60 min, the hardness increased from HV 172 of the cold-rolled state to HV 242 of the peak value. As the aging time was further prolonged, the hardness changed slightly. For aging at 500 °C, the hardness of the alloy reached the peak value (HV 239) when the aging time was 10 min. With further prolongation of the aging time, the hardness began to decrease. When the aging time exceeded 480 min, the hardness decreased to HV 215.

Taking aging at 450 °C as an example, when the aging time was 30 and 120 min, the electrical conductivity of alloy increased from 18.0% (IACS) of cold-rolled state to 38.5% (IACS) and 43.2% (IACS), respectively. As the aging time was prolonged, the electrical conductivity increased slowly. When the aging time was 240 min, the electrical conductivity increased to 43.5% IACS. Moreover, the samples aged at higher temperature had larger electrical conductivity. For the cases of aging at 400, 450 and 500 °C for 480 min, the electrical conductivities were 39.7%, 45.0% and 47.7% (IACS), respectively.

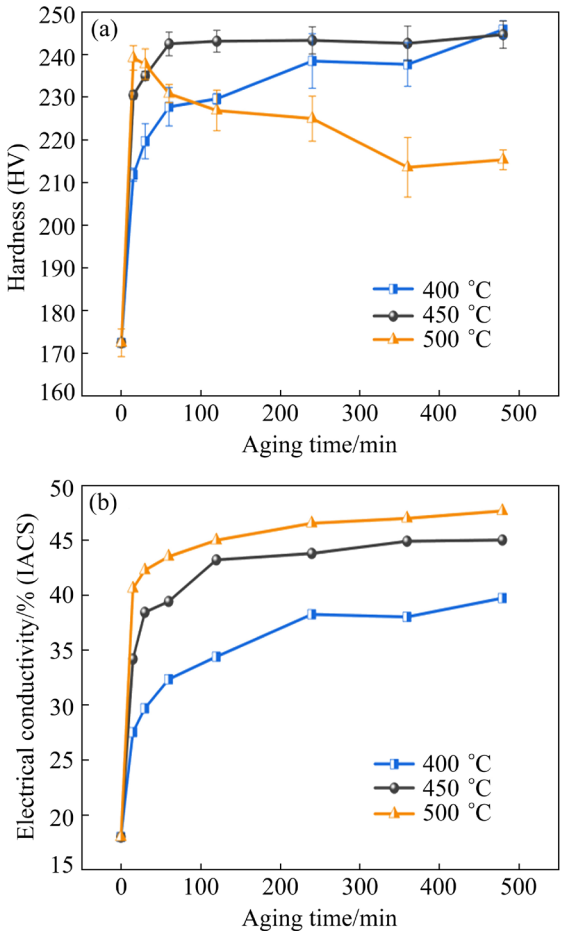


**Fig. 3** Variations of hardness (a) and electrical conductivity (b) of FTMT samples

3.1.3 Effect of STMT on properties of alloy

The alloy was treated by the STMT process (solution → 60% cold rolling → 450 °C, 1.5 h aging → 70% cold rolling →aging). Figures 4(a) and (b) show the hardness and electrical conductivity change curves of the STMT samples with aging time, respectively. The samples were aged at 350, 400 and 450 °C for different time. With prolonging the aging time, the hardness first increased and then decreased. Taking aging at 400 °C as an example, when the aging time was 0−15 min, the hardness rapidly increased from HV 244 to HV 271. When the aging time was prolonged to 120 min, the hardness increased to 274 MPa of the peak value. With further prolonging the aging time to 240 min, the hardness was reduced to HV 269. In the initial stage of aging, the electrical conductivity increased rapidly. As the aging time was prolonged, the electrical conductivity increased slowly. For the cases of aging at 350, 400 and 450 °C for 240 min, the electrical conductivity was 51.4%, 52.6% and

56.8% IACS, respectively. In addition, with increasing the aging temperature, the hardness peak value and the time needed all decreased. For aging at 350, 400 and 450 °C, the hardness peak value and the time needed were HV 278 and 240 min, HV 274 and 120 min, and HV 272 and 15 min, respectively.

3.1.4 Effect of TTMT on properties of alloy

The alloy was treated by the TTMT process (solution → 60% cold rolling → 450 °C, 1.5 h aging → 70% cold rolling → 350 °C, 0.5 h aging → 30% cold rolling → aging). Figures 5(a) and (b) show the hardness and electrical conductivity change curves of the TTMT samples with aging time, respectively. With extension of the annealing time, the hardness of the alloy first increased and then decreased, while the electrical conductivity increased. In the initial stage of aging, the hardness of the sample annealed at 300 °C was higher than that of the sample annealed at 350 °C. When the aging time exceeded 3 h, the hardness of the sample annealed at 350 °C exceeded that of the sample annealed at 300 °C. When the aging time was prolonged to 360 min, the hardness peak value reached HV 283. For the cases of aging at 300 and 350 °C for 480 min, the hardnesses of the alloy were HV 275 and HV 279, respectively. The electrical conductivities were 43.0% and 47.9% (IACS), respectively.

3.1.5 Property comparison of different treatment processes

Figure 6 shows the engineering stress−strain curves of the Cu−1.3Ni−1.2Co−0.7Si−0.3Cr−0.1Mg alloy by different treatment processes. The mechanical and electrical properties of the alloy under the peak aging stage of different heat treatments are shown in Fig. 7 and Table 3. The hardness, tensile strength, yield strength, elongation and electrical conductivity of the samples after solid solution treatment were HV 131, 334 MPa, 157 MPa, 33.4% and 46.7% (IACS), respectively. Compared with the solid solution samples, both the hardness and strength of samples treated by DAT, FTMT, STMT and TTMT were obviously improved,

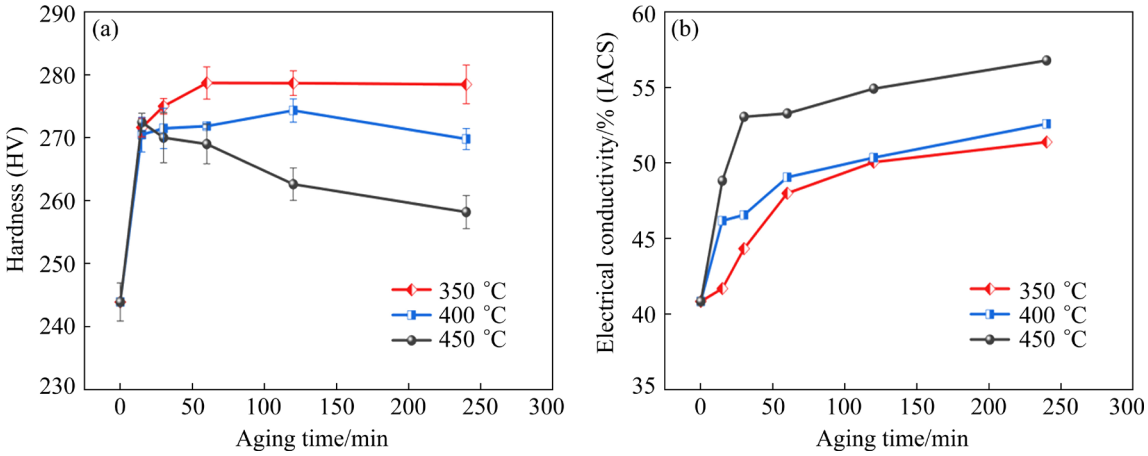


**Fig. 4** Variations of hardness (a) and electrical conductivity (b) of STMT samples

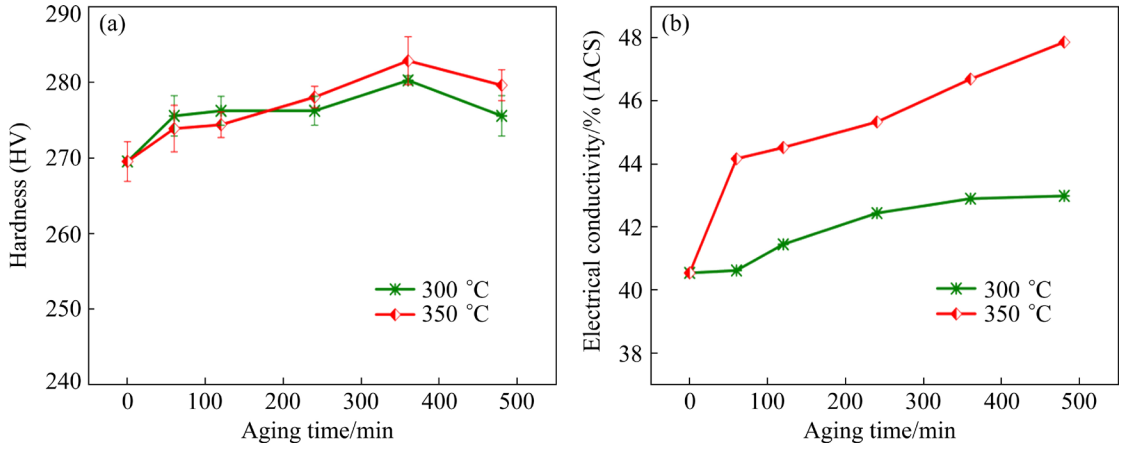


**Fig. 5** Variations of hardness (a) and electrical conductivity (b) of TTMT samples

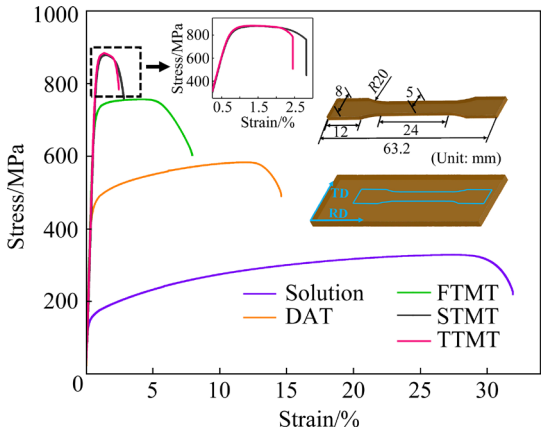


**Fig. 6** Engineering stress−strain curves of samples after different heat treatments

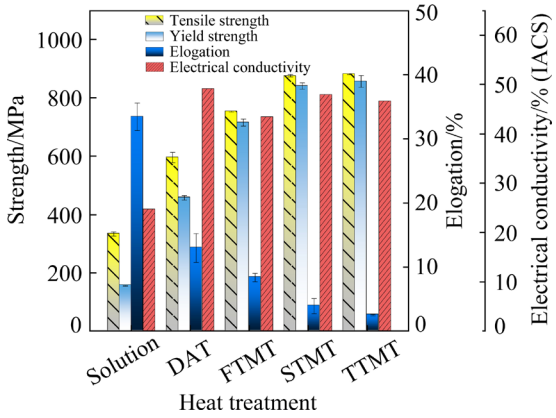


**Fig. 7** Comparisons of mechanical and electrical properties of samples

and the samples treated by STMT and TTMT had the highest hardness and strength. The DAT samples had a hardness of HV 190, tensile strength of 596 MPa, yield strength of 459 MPa, elongation of 13.0% and electrical conductivity of 49.2% IACS. Compared with the DAT samples, the hardness of the samples treated by FTMT, STMT and TTMT treatment increased by 27.9%, 46.8% and 48.9%, the tensile strength increased by 26.5%, 47.0% and 48.0%, the yield strength increased by 56.0%, 83.2% and 86.7%, the elongation decreased to 8.4%, 3.9% and 3.0%, and the electrical conductivity was 43.5%, 48.0% and 46.7% (IACS), respectively. Considering the mechanical and electrical properties of the alloy, the optimized treatment was TTMT. The hardness, tensile strength, yield strength, elongation and electrical conductivity of the alloy treated by TTMT were HV 283, 882 MPa, 857 MPa, and 3.0% and 46.7% (IACS), respectively.

### 3.2 Microstructure of Cu−1.3Ni−1.2Co−0.7Si−0.3Cr−0.1Mg alloy

#### 3.2.1 Microstructure evolution of FTMT samples

Figure 8 shows the TEM images of the alloy samples after cold rolling with a reduction of 60% and aging at 450 °C for different time. As shown in Figs. 8(a) and (b), a large number of dislocations and dislocation cells were generated in the Cu matrix after cold rolling. The dislocation walls that were formed by dislocation entanglements further hindered the movement of subsequent dislocations and improved the work hardening effect, as shown in the black cluster region in Fig. 8(c). After cold rolling, the alloy was aged at 450 °C. When the aging time was 30 min, the precipitated phases with size of 5−10 nm were formed in the alloy, as shown in Fig. 8(d). As the aging time was prolonged, the precipitated phases increased and grew, and formed nanoscale particles (Fig. 8(e)). When the aging time exceeded 600 min, the precipitated phases coarsened obviously and “sphere-like” particles formed in the matrix with size of 20−35 nm (Fig. 8(f)).

To further analyze the microstructure and composition of the alloy during aging, TEM was employed to analyze the samples after aging at 450 °C for 240 min. There were also large precipitated particles with size of 300−600 nm in

**Table 3** Comparisons of performance of samples after different heat treatments

| Process | Hardness (HV) | Electrical conductivity/% (IACS) | Tensile strength/MPa | Yield strength/MPa | Elongation/ % |
|---|---|---|---|---|---|
| Solid solution | 131 | 24.8 | 334 | 157 | 33.4 |
| DAT | 190 | 49.2 | 596 | 458 | 13.0 |
| FTMT | 243 | 43.5 | 754 | 716 | 8.4 |
| STMT | 279 | 48.0 | 876 | 841 | 3.9 |
| TTMT | 283 | 46.7 | 882 | 857 | 3.0 |

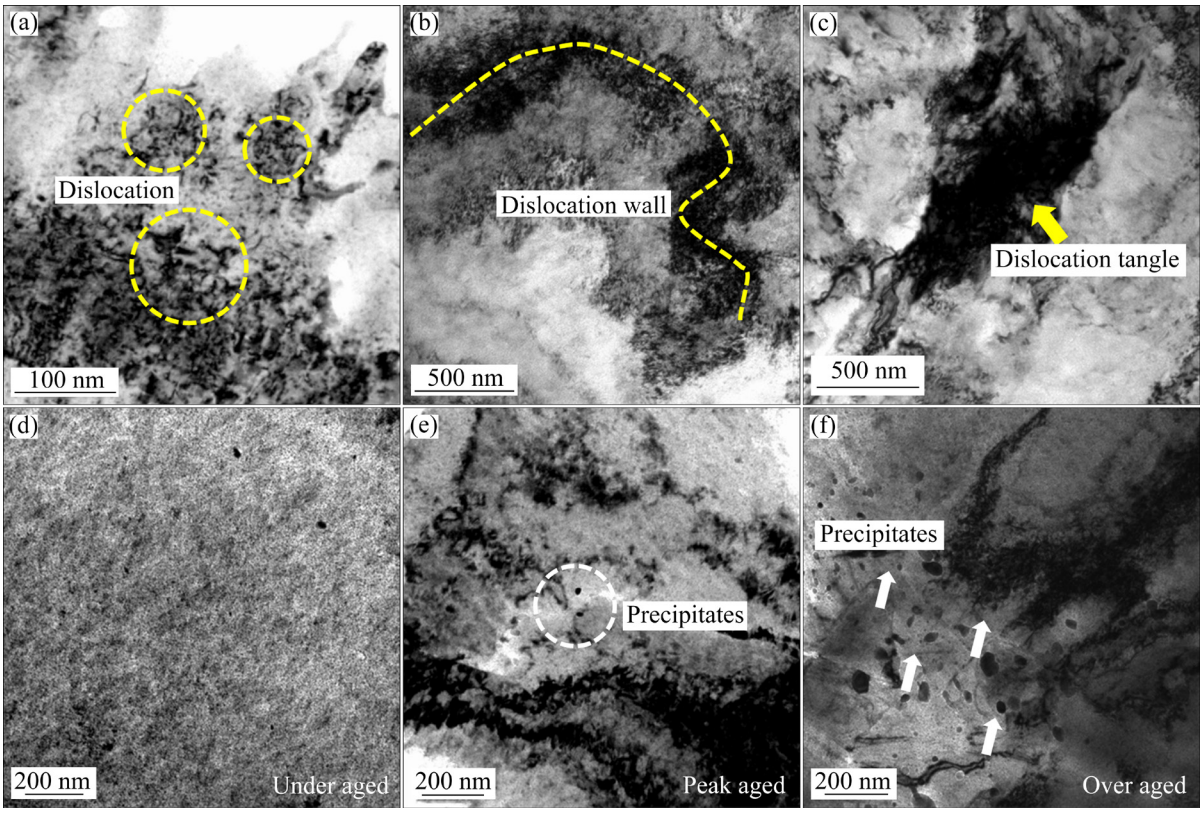


**Fig. 8** Bright-field images of FTMT samples after first-stage cold rolling and aging at 450 °C for different time: (a) Dislocation; (b) Dislocation wall; (c) Dislocation tangle; (d) Aged for 30 min; (e) Aged for 240 min; (f) Aged for 600 min

the Cu matrix, as shown in Fig. 9(a), the HRTEM of the particles can be judged to be the Cr phase. In addition, according to the energy dispersive spectrometer (EDS) analysis, except for Cu, the molar ratio of [(Ni+Co)/2+Cr/3]:Si was about 1:1. It shows that there are some $Cr_3Si$ particles in the matrix, which was the primary phase formed during solidification (Figs. 9(b) and (c)). Furthermore, a large number of nanoscale particles formed in the Cu matrix. There were apparent Moiré fringes around the particles (Figs. 9(d) and (e)). Figure 9(f) shows the diffraction pattern of the microstructure of Fig. 9(d). The incident electron beam was parallel to the axis of $[011]_{Cu}$, and the precipitated phase was determined to be $\beta$-$Ni_3Si$ phase and "sphere-like" Cr phase. According to the selected area electron diffraction (SAED) image, the $\beta$-$Ni_3Si$ and Cr phases had the following orientation relationship with the Cu matrix: $(200)_{Cu}//(100)_{\beta}//(200)_{Cr}$ and $[011]_{Cu}//[011]_{\beta}//[011]_{Cr}$, which was consistent with the reports [14,23,24]. Figure 9(g) shows nanoscale particles, and Fig. 9(h) shows the diffraction pattern of the microstructure of Fig. 9(g). The incident electron beam was parallel to the axis of $[112]_{Cu}$, and the precipitated phase was determined to be the $\delta$-$(Ni,Co)_2Si$ and $\beta$-$Ni_3Si$ phases. According to the SAED image, the phases had the following orientation relationship with the Cu matrix: $(11\bar{1})_{Cu}//(11\bar{1})_{\beta}//(220)_{\delta}$, $(2\bar{2}0)_{Cu}//(1\bar{1}0)_{\beta}//(4\bar{2}0)_{\delta}$ and $[112]_{Cu}//[112]_{\beta}//[001]_{\delta}$, which was consistent with the reports [14,25,26]. According to the above TEM results, it can be determined that the "beam-like" precipitates were $\delta$-$(Ni,Co)_2Si$ and $\beta$-$Ni_3Si$ with an orthorhombic structure and the "sphere-like" precipitates were Cr phases.

3.2.2 Microstructure evolution of STMT samples

Figure 10 shows the TEM images of the alloy samples after cold rolling with a reduction of 70% and aging at 350 °C for 60 min. From Figs. 10(a) and (b), the number of dislocations in the alloy was further increased after cold rolling, and a large number of dislocations accumulated and interacted to form sub-grains such as dislocation cells. The precipitates that were formed during the first-stage aging pinned up the dislocations which were formed

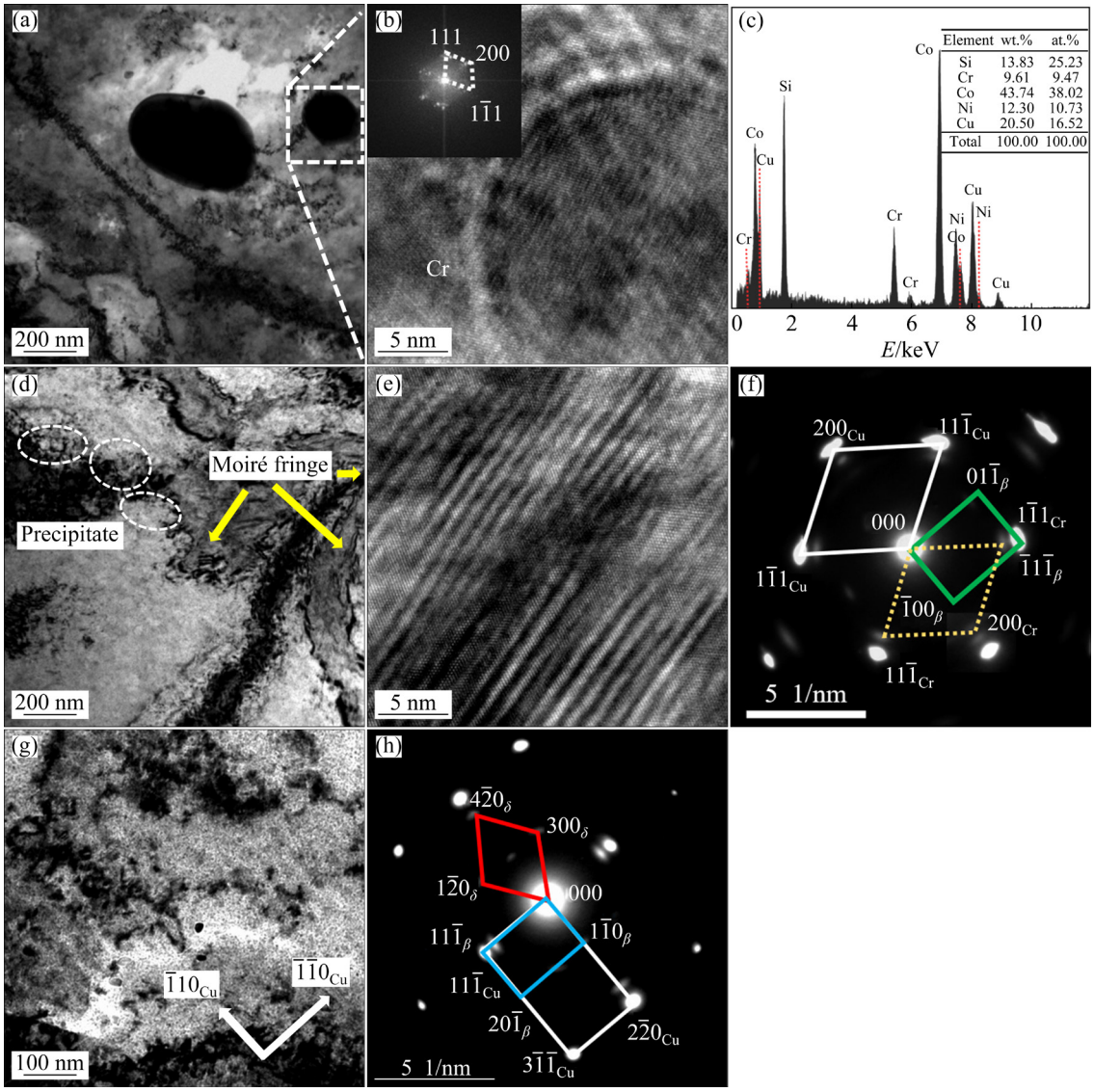


**Fig. 9** Bright-field images of FTMT samples after aging at 450 °C for 240 min: (a) Cr particle; (b) HRTEM of (a); (c) EDS of (a); (d) Precipitates and Moiré fringes; (e) HRTEM of Moiré fringes; (f) SAED of (d), beam direction along $[011]_{Cu}$; (g) Precipitates; (h) SAED of (g), with beam direction along $[112]_{Cu}$

during the second-stage cold rolling (see Fig. 10(c)), and the interaction between precipitated particles and dislocations further improved the strain strengthening effect. There were also a large number of dislocation entanglements around the $Cr_3Si$ phase in the alloy, as shown in Fig. 10(d). After the second-stage aging, a large number of precipitated phases continued to nucleate around the high-density dislocations, and formed dispersed particles with size of 10−30 nm, as shown in Figs. 10(e) and (f)). According to the SAED image, the nanoscale precipitated phase in the Cu matrix was $\beta$-$Ni_3Si$, which had the following orientation relationship with the Cu matrix: $(200)_{Cu}//(100)_{\beta}$ and $[011]_{Cu}//[011]_{\beta}$.

3.2.3 Microstructure evolution of TTMT samples

Figure 11 shows the TEM images of the alloy samples after cold rolling with a reduction of 30% and aging at 350 °C for 360 min. From Figs. 11(a−c), the samples treated by third-stage cold rolling had higher density dislocations and more dislocation cells than the STMT sample. However, different sign dislocations accumulated and cancelled each other, which resulted in dislocation annihilation, so that the effect of work hardening was not significant in the alloy. In addition, after annealing at 350 °C for 360 min, a large number of 20−40 nm phase particles continued to precipitate in the high-density dislocation regions and along the sub-grain boundaries. According to

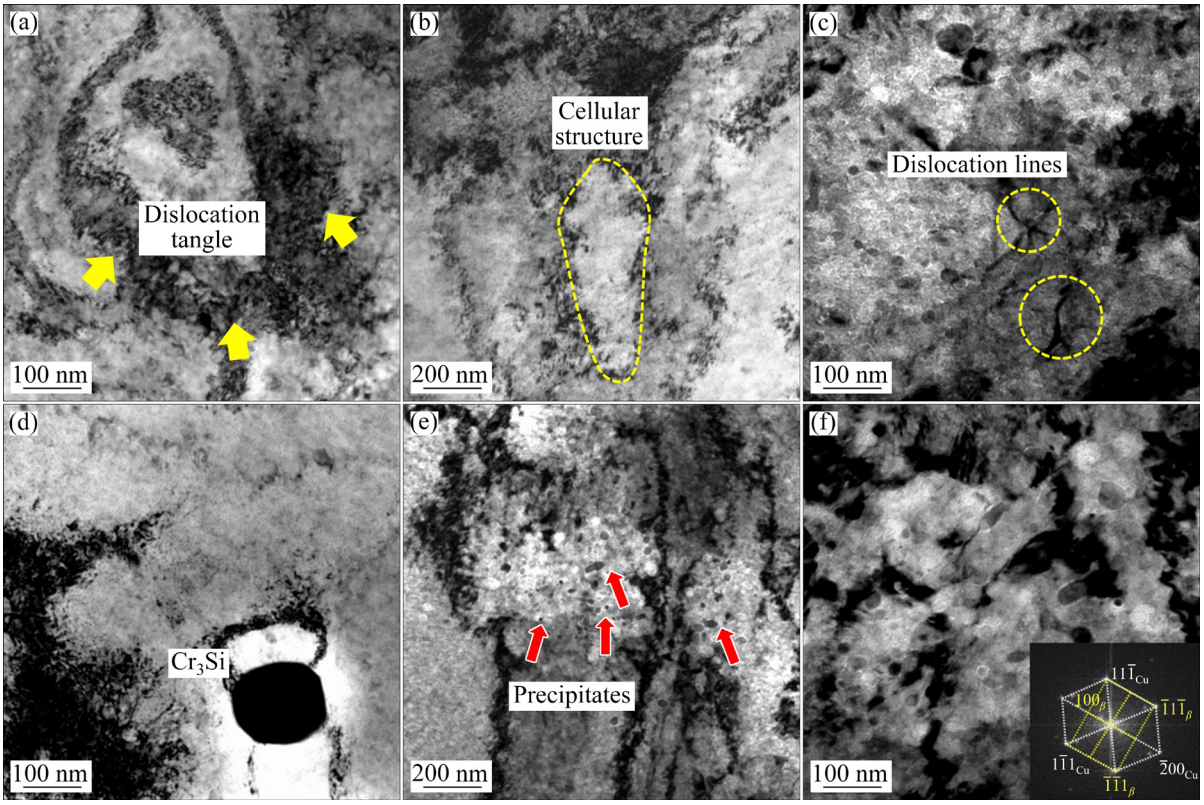


**Fig. 10** Bright-field TEM images of STMT samples: (a−c) After cold rolling by 70%; (d−f) After aging at 350 °C for 60 min

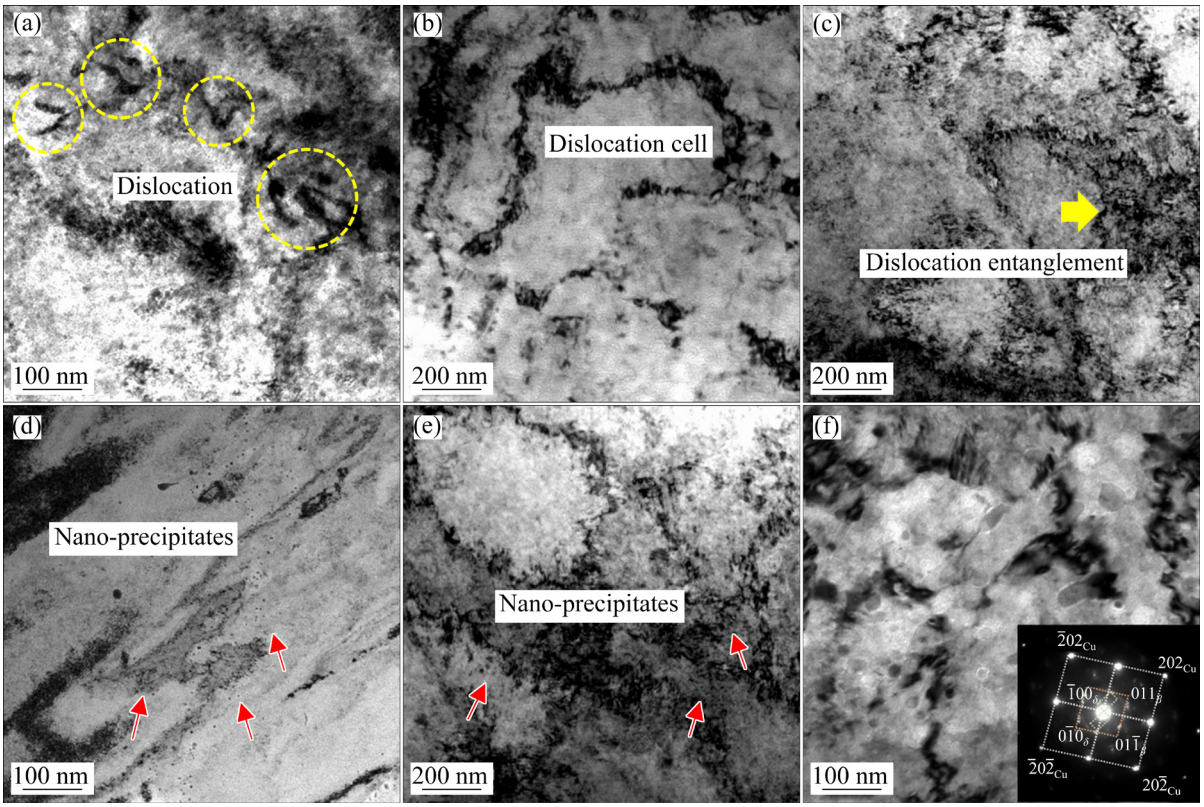


**Fig. 11** Bright-field TEM images of TTMT samples: (a−c) After cold rolling by 30%; (d−f) After aging at 350 °C for 360 min

the SAED image, the nanoscale precipitated phases in the Cu matrix were $\delta$-$(Ni,Co)_2Si$ and $\beta$-$Ni_3Si$, and the interaction between precipitated phases and dislocations improved (Figs. 11(d−f)).

## 4 Discussion

A Cu−1.3Ni−1.2Co−0.7Si−0.3Cr−0.1Mg alloy was prepared by different treatments in this work. According to the above experimental results, the strength and electrical conductivity of the samples treated by the TTMT and STMT were higher than those of the samples treated by the DAT and FTMT, and the TTMT samples had the highest strength and relatively high electrical conductivity among them. The hardness, tensile strength, yield strength, elongation and electrical conductivity of the alloy were HV 283, 882 MPa, 857 MPa, 3.0% and 46.7% (IACS), respectively. The dislocation configuration of the Cu matrix, the precipitation behavior of the strengthening phases and the interaction between them had significant impact on the strength and electrical conductivity of the alloy during thermomechanical treatment.

### 4.1 Precipitation behavior of Cu−1.3Ni−1.2Co−0.7Si−0.3Cr−0.1Mg alloy and its effect on properties

Cu−Ni−Co−Si alloy is a typical aging precipitation strengthening alloy. In the early stage of aging, due to the strong binding force of Si and Co atoms in the Cu matrix, they preferentially combined to form $Co_2Si$ phase, and then Si and Ni atoms combined to form $Ni_2Si$ phase [5]. With extension of aging time, the number of $Co_2Si$ and $Ni_2Si$ phases increased. Because the formation enthalpy and crystal structure of $Co_2Si$ were very close to those of $Ni_2Si$, they precipitated in the form of a continuous solid solution $(Ni,Co)_2Si$ phase [27]. The $(Ni,Co)_2Si$ phase induced a large lattice distortion in the Cu matrix, which produced great effects of pinning dislocations and strengthening [28,29]. Adding Cr element to Cu−Ni−Co−Si alloy and keeping low content of Ni and Co elements, on the one hand, it was helpful to controlling the high cost of precious metal Co. On the other hand, the decrease of electrical conductivity due to the infinite miscibility between Ni and matrix Cu can also be controlled. Meanwhile, nanoscale Cr phase particles formed due to addition of Cr element (see Figs. 9(d−f)), which greatly increased the content of precipitated phase in the matrix and helped to strengthen the matrix. The addition of Mg element can not only produce solid solution strengthening, but also pin dislocations and effectively improve the stress relaxation rate of alloy [30].

The samples after solid solution treatment were subjected to the first-stage cold rolling with a reduction of 60% during the multistage thermo-mechanical treatment. A large number of dislocations and sub-grains were generated in the Cu matrix (see Figs. 8(a−c)), which not only provided more nucleation positions for precipitated phases during the subsequent aging but also promoted the diffusion of Ni, Co and Si elements and accelerated the precipitation of the second phases. The alloy was aged at 450 °C after the first-stage cold rolling. In the initial stage of aging, there was a large precipitation driving force and a fast precipitation speed in the alloy due to the high content of solute atoms (Ni, Co and Si) in the alloy. Therefore, a large number of nanoscale $(Ni,Co)_2Si$ phase particles precipitated in the Cu matrix, which increased the hardness of the alloy (see Fig. 8(d)). As the aging time was prolonged, the number of $(Ni,Co)_2Si$, $Ni_3Si$ and Cr phase particles increased, and there were bright and dark Moiré fringes around the precipitated phases (see Fig. 9), which hindered dislocation movement and effectively improved the hardness. Meanwhile, some submicron $Cr_3Si$ phase particles formed during solidification can effectively pin the movement of grain boundary and improve the high temperature softening resistance of the alloy [31]. When the aging time was 240 min, both the hardness and strength of the alloy reached the peak value, and the hardness, tensile strength, yield strength and electrical conductivity of the alloy were HV 243, 754 MPa, 716 MPa and 43.5% (IACS), respectively. When the aging time was further prolonged, the precipitated phases coarsened, and the strengthening effect and hardness of the alloy decreased. In addition, the alloy elements in the Cu matrix continued to precipitate, and the electrical conductivity showed an upward trend (see Fig. 3).

The under-aged samples in the FTMT process were subjected to the second-stage cold rolling with a reduction of 70%. On the one hand, a large number of dislocations and sub-grains formed in the alloy (see Fig. 10(a−c)). Furthermore, the

precipitated phases that formed during under-aged can effectively pin-up the dislocation movement. The strong interaction between precipitated phases and dislocations was conducive to further increasing the dislocation density of the alloy, improving the strain strengthening effect and promoting the subsequent aging precipitation. The $(Ni,Co)_2Si$, $Ni_3Si$ and Cr phases were further dispersedly precipitated in the high-density dislocation region of the Cu matrix during the second-stage aging. As shown in Figs. 10(d−f), the interaction between dislocations and precipitated phases further increased, and the strengthening effect was remarkable, which further improved the hardness, strength and electrical conductivity of the alloy. The hardness, tensile strength, yield strength and electrical conductivity of the alloy were HV 279, 876 MPa, 841 MPa and 48.0% (IACS), respectively (see Fig. 4). In the STMT process, the best aging parameters were 350 °C, 1 h (peak-aging stage). But in the actual production, it was easy to crack when selecting the peak-aged sample of large billet sheet and strip for rolling, which was not conducive to the processing performance. Therefore, the TTMT process adopted 350 °C, 0.5 h (under-aging state) for heat treatment.

The STMT samples were subjected to the third-stage cold rolling with a reduction of 30%. A large number of dispersed precipitates were produced during the first-stage under-aging and second-stage peak-aging. A stronger interaction between dislocations and precipitated phases was generated, which further increased the number of dislocations and sub-grains (see Fig. 11(a−c)). Meanwhile, the third-stage treatment process used low-temperature and long-term annealing (350 °C, 360 min), which was benefit for reducing the residual stress of the alloy. On the other hand, the Ni, Co, Cr and Si atoms in the Cu matrix continued to precipitate in the form of $(Ni,Co)_2Si$, $Ni_3Si$ and Cr phases in the high-density dislocation regions and along the sub-grain boundaries (Figs. 11(d−f)), which enhanced the strengthening effect. On the basis of maintaining good electrical conductivity, both the hardness and strength of the alloy were further improved. The hardness, tensile strength, yield strength and electrical conductivity of the prepared alloy were HV 283, 882 MPa, 857 MPa and 46.7% (IACS), respectively (see Fig. 5).

Besides, through the multistage thermo-mechanical treatment process, the phase transformation storage energy was improved. A large number of dislocation entanglements and substructures formed in the Cu matrix, and the precipitation of solute atom was fully promoted. The contents of alloy elements which dissolved into the Cu matrix were significantly decreased, which reduced electron scattering and rapidly enhanced the electrical conductivity.

### 4.2 Strengthening mechanism

According to the above microstructure analysis, the high strength of the Cu−1.3Ni−1.2Co−0.7Si−0.3Cr−0.1Mg alloy prepared in this work was mainly attributed to precipitation strengthening, strain strengthening, sub-grain strengthening and solid-solution strengthening. To further analyze the effect of microstructure on the strength of the alloy, the contribution of different strengthening mechanisms on the yield strength of the alloy was calculated. Finally, the total strength of the alloy was obtained by the linear superposition method. The parameters used for the strength are listed in Table 4.

#### 4.2.1 Precipitation strengthening

Precipitation strengthening is one of the significant strengthening mechanisms of high-performance copper alloys, and the main strengthening mechanism is the Orowan bypass mechanism, which is achieved by the interaction of elastic strain energy and dislocations [34]. The yield strength resulted from the Orowan bypass mechanism can be expressed by Eq. (1) [35,36]:

**Table 4** Parameters of strengthening mechanism

| Parameter | Description | Value | Ref. |
|---|---|---|---|
| $M$ | Taylor factor | 3.1 | [26] |
| $b$/nm | Burgers vector magnitude | 0.2556 | [5] |
| $v$ | Poisson's ratio | 0.34 | [5] |
| $G$/GPa | Shear modulus of matrix | 48 | [26] |
| $K_y$/(MPa·μm$^{1/2}$) | Hall−Petch coefficient | 150 | [5] |
| $\alpha$ | Constant | 0.3 | [26] |
| $\sigma_0$/MPa | Intrinsic lattice strength | 60 | [32] |
| $\delta_{Ni}$ | Factor of lattice change | 0.032 | [33] |
| $\delta_{Cr}$ | | 0.0618 | [33] |
| $\delta_{Mg}$ | | 0.1467 | [33] |

$$\Delta\sigma_{or}=\frac{0.81MGb}{2\pi(1-\nu)^{1/2}}\cdot\frac{\ln(d_p/b)}{\lambda-d_p} \quad (1)$$

where $d_p$ is the average size of the precipitated phases (measured from eight TEM micrographs of the samples in peak aging stage during different heat treatment by Image-Pro Plus software in this work), $\lambda$ is the average spacing between precipitates, and $f_v$ is the average volume fraction of precipitated phases. The yield strength resulted from precipitation strengthening can be expressed by Eq. (2) [37]:

$$\lambda=d_p\sqrt{\frac{3\pi}{8f_v}} \quad (2)$$

The distribution histogram of precipitations size is shown in Fig. 12. From the intercept distribution, it can be deduced that the average precipitations size of FTMT specimens is (13.1±7.4) nm, the average precipitation size of STMT samples is (9.4±2.3) nm and the average precipitation size of TTMT samples is (9.3±1.5) nm. The calculated strength values of precipitation strengthening of the alloy prepared by different treatments are listed in Table 5.

4.2.2 Strain strengthening

Cold working greatly produces dislocations, and the cutting stress and bypass stress of dislocations also increase. To promote nucleation and precipitation and add the deformation energy storage of the Cu matrix, multistage rolling was designed, and the yield strength produced by strain strengthening was calculated by Eq. (3) [38]:

$$\Delta\sigma_{Dis}=M\alpha Gb\rho^{1/2} \quad (3)$$

where $\rho$ is the dislocation density, and $\varepsilon$ is the micro-strain. Dislocation density ($\rho$) can be expressed by Eq. (4) [39]:

$$\rho=\frac{16.1\varepsilon^2}{b^2} \quad (4)$$

The XRD patterns of samples and diffraction peak broadening $\beta\cos\theta$ as a function of $4\sin\theta$ are shown in Fig. 13. The calculated strength produced by the strain strengthening of alloys prepared by different treatments is shown in Table 6. Peaks explicitly representing the Cu phase can be observed in all samples under different treatments. The dislocation density of the samples under different treatments is generally estimated based on

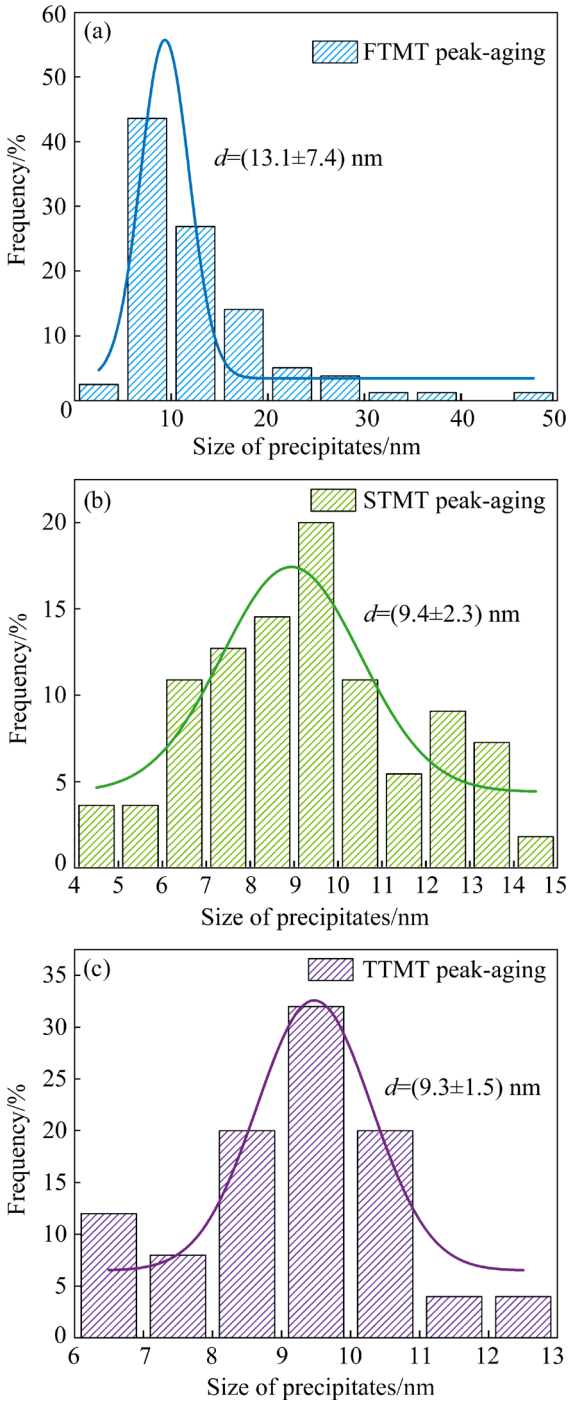


**Fig. 12** Distribution histogram of precipitates size with different treatment processes: (a) FTMT; (b) STMT; (c) TTMT

**Table 5** Parameters and calculated results of precipitation strengthening

| Process | $d_p$/ nm | $f_v$/ % | $M$ | $G$/ GPa | $b$/ nm | $\nu$ | $\Delta\sigma_{or}$/ MPa |
|---|---|---|---|---|---|---|---|
| FTMT | 13.1 | 4.19 | 3.1 | 48 | 0.2556 | 0.34 | 425.7 |
| STMT | 9.4 | 4.27 | 3.1 | 48 | 0.2556 | 0.34 | 549.6 |
| TTMT | 9.3 | 4.28 | 3.1 | 48 | 0.2556 | 0.34 | 554.7 |

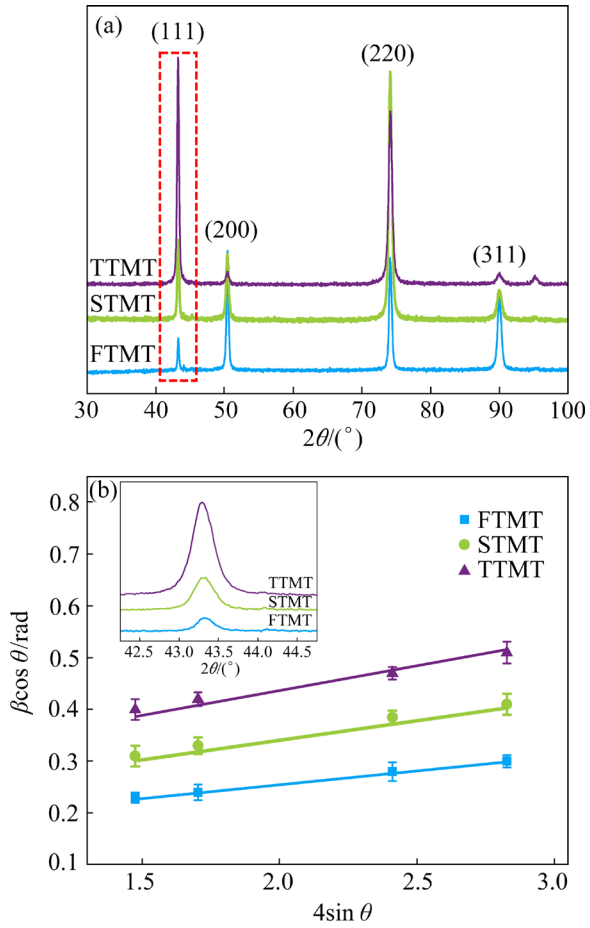


**Fig. 13** (a) XRD patterns of samples by FTMT, STMT, and TTMT treatment; (b) Upper-left area: local magnification of diffraction peak in red frame of (a), lower-right area: peak broadening $\beta\cos\theta$ as function of $4\sin\theta$ by FTMT, STMT and TTMT treatment (calculated by (a))

**Table 6** Parameters and calculated results of strain strengthening

| Process | $\rho$/m$^{-2}$ | $M$ | $\alpha$ | $G$/GPa | $b$/nm | $\Delta\sigma_{Dis}$/MPa |
|---|---|---|---|---|---|---|
| FTMT | $6.83\times10^{13}$ | 3.1 | 0.3 | 48 | 0.2556 | 94.3 |
| STMT | $1.05\times10^{14}$ | 3.1 | 0.3 | 48 | 0.2556 | 116.9 |
| TTMT | $1.28\times10^{14}$ | 3.1 | 0.3 | 48 | 0.2556 | 129.1 |

the Williamson−Hall method. The peak broadening $\beta\cos\theta$ and $4\sin\theta$ of the diffraction peak can be obtained from the XRD pattern. $\beta\cos\theta$ and $4\sin\theta$ are taken as the vertical and horizontal axes of the coordinate axes, respectively. The slope of the fitted lines represents the micro-strain ($\varepsilon$), which is 0.053 for the FTMT specimen, 0.065 for the STMT specimen, and 0.072 for the TTMT specimen.

4.2.3 Sub-grain strengthening

Cold working introduced a large number of sub-grains such as dislocation cells, so that the grain size decreased and the grain boundary area increased, which hindered dislocation movement and improved the yield stress. The yield strength can be calculated by Hall−Patch as Eq. (5) [40]:

$$\Delta\sigma_{GB}=K_y/\sqrt{d_g} \tag{5}$$

where $K_y$ is estimated to be 150, indicating the effect of surrounding grains on flow resistance, and $d_g$ is the average diameter of grain in the Cu matrix (measured from eight TEM micrographs of the samples in peak aging stage during different heat treatments by Image-Pro Plus software in this work). The distribution histogram of grain size is shown in Fig. 14. From the intercept distribution, it can be deduced that the average grain size of FTMT samples is (3.46±0.34) μm, the average grain size of STMT specimens is (2.07±0.46) μm and the average grain size of TTMT specimens is (1.95±0.36) μm. The yield strength produced by the sub-grain strengthening of the alloys prepared by different treatments is shown in Table 7.

4.2.4 Solid-solution strengthening

Different solute atoms and Cu atoms have different atomic radius and shear modulus. When the alloying elements are dissolved into Cu matrix, lattice distortion in the matrix occurs, resulting in a strengthening effect. In addition, the dislocation line energy varies with different shear modulus. Because Cu, Mg and Cr atoms are of the same scale, the addition of Mg and Cr elements can strengthen the Cu matrix by forming an alternative solid solution. Ni and Cu are infinitely miscible systems that produce a large solid solubility in the matrix, which causes a strengthening effect. In this work, assuming that all Co and Si elements fully precipitate in the form of the second phase, only the contribution of Ni, Cr and Mg elements to the yield strength is considered, which is calculated by Eq. (6) [41]:

$$\Delta\sigma_s=\sum G\delta x_a^{3/2}\sqrt{\frac{x_a}{3}} \tag{6}$$

where $\delta$ is the lattice change factor, which is related to the type of elements, and $x_a$ is the molar fraction of solute atom. The yield strength produced by the solid-solution strengthening of alloys prepared by different treatment processes is shown in Table 8.

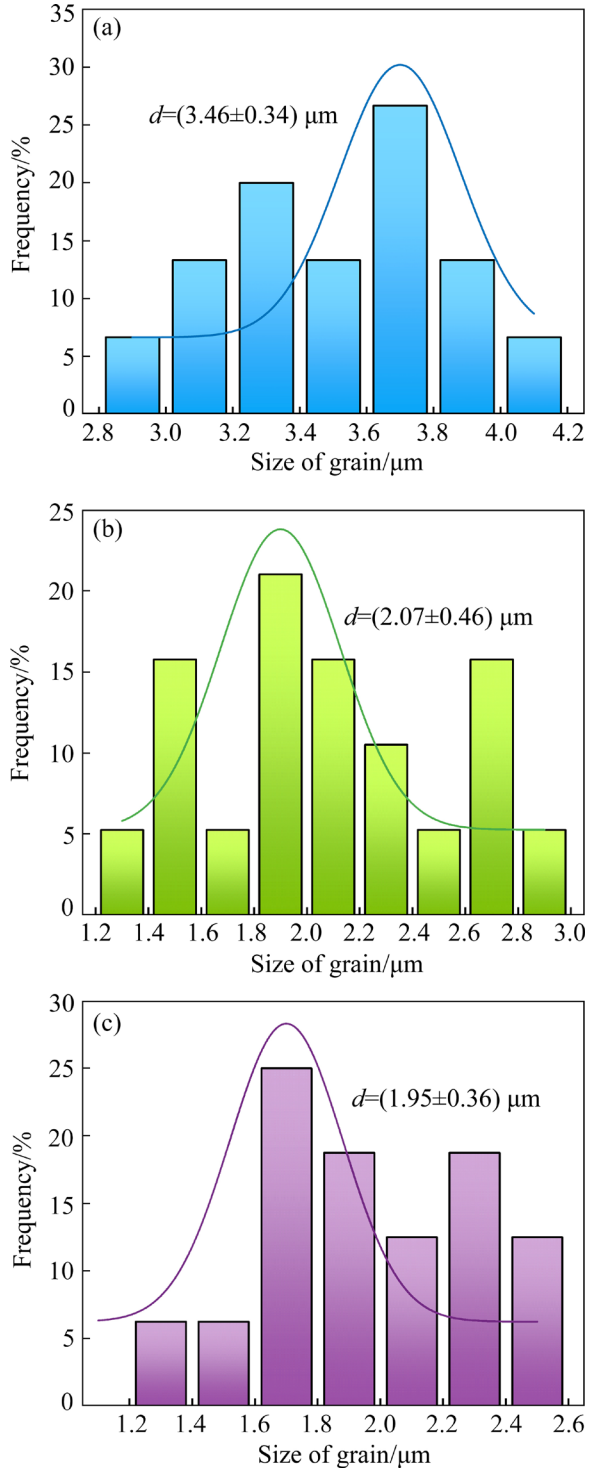


**Fig. 14** Distribution histogram of grains size by different treatment processes: (a) FTMT; (b) STMT; (c) TTMT

**Table 7** Parameters and calculated results of sub-grain strengthening

| Process | $d_g$/μm | $K_y$/(MPa·μm$^{1/2}$) | $\Delta\sigma_{GB}$/MPa |
|---|---|---|---|
| FTMT | 3.46 | 150 | 80.6 |
| STMT | 2.07 | 150 | 104.3 |
| TTMT | 1.95 | 150 | 107.4 |

The total strength of the alloy can be calculated by Eq. (7) [42,43]:

$$\sigma_{total}=\sigma_0+\Delta\sigma_{or}+\Delta\sigma_{Dis}+\Delta\sigma_{GB}+\Delta\sigma_s \quad (7)$$

where $\sigma_0$ is estimated to be 60 MPa. Table 9 lists the contribution of yield strength to each strengthening mechanism of the alloy under different treatment conditions as well as the deviation between the experimental and calculated data. The deviations for the FTMT, STMT and TTMT samples were 8.0%, 0.93% and 1.2%, respectively. Taking the TTMT sample as an example, the strengthening contributions of the alloy from large to small were precipitation strengthening, strain strengthening, sub-grain strengthening and solid-solution strengthening, which were 65%, 15%, 12.7% and 0.3%, respectively. The main strengthening mechanisms of alloys are precipitation strengthening, strain strengthening and sub-grain strengthening.

Figure 15 shows the comparison of tensile strength and electrical conductivity among the Cu−Ni−Co−Si−Cr−Mg alloy studied in this work and the Cu−Zn−Sn, Cu−Sn, Cu−Mg, Cu−Be, Cu−Ti, Cu−Zr, Cu−Cr, Cu−Cr−Zr, Cu−Ni−Si and other alloys. In this work, proper contents of Co, Cr and Mg elements were added to a Cu−Ni−Si alloy to strengthen the interaction between precipitates and dislocations by the synergistic effects of various alloy elements and controlling of the thermo-mechanical treatment. Reasonable matching of the high strength (>850 MPa) and medium electrical conductivity (>45% (IACS)) of copper alloy was achieved through comprehensive effects of precipitation strengthening, strain strengthening,

**Table 8** Relevant parameters and calculated results of solid-solution strengthening

| Process | $\delta_{Ni}$ | $\delta_{Cr}$ | $\delta_{Mg}$ | $x_{Ni}$ | $x_{Cr}$ | $x_{Mg}$ | $G$/GPa | $\Delta\sigma_s$/MPa |
|---|---|---|---|---|---|---|---|---|
| FTMT | 0.032 | 0.0618 | 0.1467 | 1.421293 | 0.313634 | 0.335482 | 48 | 2.42 |
| STMT | 0.032 | 0.0618 | 0.1467 | 1.421293 | 0.313634 | 0.335482 | 48 | 2.42 |
| TTMT | 0.032 | 0.0618 | 0.1467 | 1.421293 | 0.313634 | 0.335482 | 48 | 2.42 |

**Table 9** Comparison of experimental and calculated values of yield strength under different heat treatments

| Process | $\sigma_0$/MPa | $\Delta\sigma_{or}$/MPa | $\Delta\sigma_{Dis}$/MPa | $\Delta\sigma_{GB}$/MPa | $\Delta\sigma_s$/MPa | $\sigma_{total}$/MPa | $\sigma_{exp}$/MPa | $\sigma_{err}$/% |
|---|---|---|---|---|---|---|---|---|
| FTMT | 60 | 425.7 | 94.3 | 80.6 | 2.42 | 663.1 | 716 | 8.0 |
| STMT | 60 | 549.6 | 116.9 | 104.3 | 2.42 | 833.2 | 841 | 0.93 |
| TTMT | 60 | 554.7 | 129.1 | 107.4 | 2.42 | 853.6 | 857 | 0.4 |

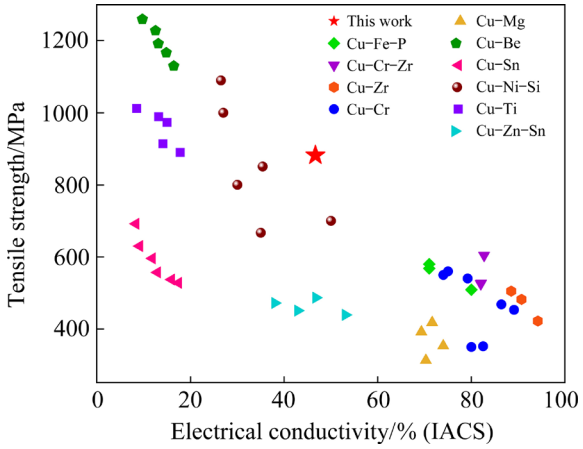


**Fig. 15** Properties of copper alloys with different compositions

sub-grain strengthening. The prepared alloy had hardness of HV 283, tensile strength of 882 MPa, yield strength of 857 MPa, and electrical conductivity of 46.7% (IACS).

## 5 Conclusions

(1) A Cu−1.3Ni−1.2Co−0.7Si−0.3Cr−0.1Mg alloy with high strength and medium conductivity was designed and multistage thermomechanical treatment was proposed, i.e., solid solution treating at 940 °C for 90 min→ cold rolling by 60%→ aging at 450 °C for 90 min→ cold rolling by 70%→ aging at 350 °C for 30 min→ cold rolling by 30% → annealing at 350 °C for 300 min. The hardness, tensile strength, yield strength and electrical conductivity of the prepared alloy were HV 283, 882 MPa, 857 MPa and 46.7% (IACS), respectively.

(2) A large number of nanoscale $\beta$-$Ni_3Si$, $\delta$-$(Ni,Co)_2Si$ and Cr phase particles precipitated in the high-density dislocation region and along the sub-grain boundaries during aging, and submicron $Cr_3Si$ phase particles formed during solidification of the alloy. Thus, the synergistic effect of multi-phase and multi-scale particles can be played to strengthen the matrix and improve the electrical conductivity. The $\beta$-$Ni_3Si$ and $\delta$-$(Ni,Co)_2Si$ phases had the following orientation relationship with the Cu matrix: $[112]_{Cu}//[112]_\beta//[001]_\delta$, $(11\bar{1})_{Cu}//(11\bar{1})_\beta//(220)_\delta$ and $(2\bar{2}0)_{Cu}//(1\bar{1}0)_\beta//(4\bar{2}0)_\delta$; $[011]_{Cu}//[011]_\beta$, $(200)_{Cu}//(100)_\beta$.

(3) The strengthening mechanisms of the Cu−1.3Ni−1.2Co−0.7Si−0.3Cr−0.1Mg alloy by multistage thermomechanical treatments were precipitation strengthening, strain strengthening, sub-structure strengthening and solid-solution strengthening. The yield strength values calculated by strengthening model were 554, 129, 107 and 2.4 MPa, respectively. The main strengthening mechanisms of the alloy were precipitation strengthening, strain strengthening and sub-grain strengthening.

## Acknowledgments

This work was supported by the National Key Research and Development Program of China (No. 2020YFB0311102), and the Ningbo "Science and Technology Innovation 2025" Major Project, China (No. 2019B10087).

## References

[1] AZZEDDINE H, BAUDIN T, HELBERT A L, BRISSET F, HUANG Y, KAWASAKI M, BRADAI D, LANGDON T G. A stored energy analysis of grains with shear texture orientations in Cu−Ni−Si and Fe−Ni alloys processed by high-pressure torsion [J]. Journal of Alloys and Compounds, 2021, 864: 158142.

[2] HUA Y H, NIE Z H, WANG L, ZHANG H, WANG C L, TAN C W, WANG Y D. Studies of intergranular and intragranular stresses in cold-rolled CuNiSi alloys [J]. Journal of Alloys and Compounds, 2020, 818: 152896.

[3] SEMBOSHI S, SATO S, IWASE A, TAKASUGI T. Discontinuous precipitates in age-hardening CuNiSi alloys [J]. Materials Characterization, 2016, 115: 39−45.

[4] SHEN L N, LI Z, ZHAO Y Y, WANG Y, DONG Q Y, WANG M Y. Phase transformation behavior of Cu−10Ni−3Al−0.8Si alloy [J]. Materials Chemistry and Physics, 2016, 173: 421−428.

[5] LI J, HUANG G J, MI X J, PENG L J, XIE H F, KANG Y L. Microstructure evolution and properties of a quaternary Cu−Ni−Co−Si alloy with high strength and conductivity [J]. Materials Science and Engineering A, 2019, 766: 138390.

[6] LEI Q, LI Z, GAO Y, PENG X, DERBY B. Microstructure and mechanical properties of a high strength Cu−Ni−Si alloy treated by combined aging processes [J]. Journal of Alloys and Compounds, 2017, 695: 2413−2423.

[7] SUZUKI S, SHIBUTANI N, MIMURA K, ISSHIKI M, WASEDA Y. Improvement in strength and electrical conductivity of Cu−Ni−Si alloys by aging and cold rolling [J]. Journal of Alloys and Compounds, 2006, 417(1/2): 116−120.

[8] YANG H Y, MA Z C, LEI C H, MENG L, FANG Y T, LIU J B, WANG H T. High strength and high conductivity Cu alloys: A review [J]. Science China Technological Sciences, 2020, 63(12): 2505−2517.

[9] TANG S K, LI Z, GONG S, XIAO Z. Mechanical property and corrosion behavior of aged Cu−20Ni−20Mn alloy with ultra-high strength [J]. Journal of Central South University, 2020, 27(4): 1158−1167.

[10] PAN Zhen-ya, CHEN Jiang-biao, LI Jin-fu. Microstructure and properties of rare earth-containing Cu−Cr−Zr alloy [J]. Transactions of Nonferrous Metals Society of China, 2015, 25(4): 1206−1214.

[11] WANG Meng, YANG Qian-ru, JIANG Yan-bin, LI Zhou, XIAO Zhu, GONG Shen, WANG Yong-ru, GUO Chuang-li, WEI Hai-gen. Effects of Fe content on microstructure and properties of Cu−Fe alloy [J]. Transactions of Nonferrous Metals Society of China, 2021, 31(10): 3039−3049.

[12] SUN W, XU H, LIU S, DU Y, YUAN Z, HUANG B. Phase equilibria of the Cu−Ni−Si system at 700 °C [J]. Journal of Alloys and Compounds, 2011, 509(41): 9776−9781.

[13] GHOLAMI M, VESELY J, ALTENBERGER I, KUHN H A, JANECEK M, WOLLMANN M, WAGNER L. Effects of microstructure on mechanical properties of CuNiSi alloys [J]. Journal of Alloys and Compounds, 2017, 696: 201−212.

[14] ZHAO Z, ZHANG Y, TIAN B H, JIA Y L, LIU Y, SONG K X, VOLINSKY A A. Co effects on Cu−Ni−Si alloys microstructure and physical properties [J]. Journal of Alloys and Compounds, 2019, 797: 1327−1337.

[15] XIAO X P, YI Z Y, CHEN T T, LIU R Q, WANG H. Suppressing spinodal decomposition by adding Co into Cu−Ni−Si alloy [J]. Journal of Alloys and Compounds, 2016, 660: 178−183.

[16] MONZEN R, WATANABE C. Microstructure and mechanical properties of Cu−Ni−Si alloys [J]. Materials Science and Engineering A, 2008, 483/484: 117−119.

[17] XIAO T, SHENG X F, LEI Q, ZHU J L, LI S Y, LIU Z R, LI Z. Effect of magnesium on microstructure refinements and properties enhancements in high-strength CuNiSi alloys [J]. Acta Metallurgica Sinica (English Letters), 2020, 33(3): 375−384.

[18] WANG W, KANG H J, CHEN Z N, CHEN Z J, ZOU C L, LI R G, YIN G M, WANG T M. Effects of Cr and Zr additions on microstructure and properties of Cu−Ni−Si alloys [J]. Materials Science and Engineering A, 2016, 673: 378−390.

[19] JIA Y L, WANG M P, CHEN C, DONG Q Y, WANG S, LI Z. Orientation and diffraction patterns of $\delta$-$Ni_2Si$ precipitates in Cu−Ni−Si alloy [J]. Journal of Alloys and Compounds, 2013, 557: 147−151.

[20] DONG Q, WANG M, JIA Y, LI Z, XIA C, LEI Q. Effect of thermomechanical treatment on microstructure and properties of Cu−1.5Ni−0.34Si alloy [J]. Materials Science and Engineering of Powder Metallurgy, 2011, 16(4): 531−536. (in Chinese)

[21] ZHAO D M, DONG Q M, LIU P, KANG B X, HUANG J L, JIN Z H. Aging behavior of Cu−Ni−Si alloy [J]. Materials Science and Engineering A, 2003, 361(1/2): 93−99.

[22] LEI J G, HUANG J L, LIU P D, JING X T, ZHAO D M, ZHI X. The effects of aging precipitation on the recrystallization of CuNiSiCr alloy [J]. Journal of Wuhan University of Technology: Mater Sci Ed, 2005, 20(1): 21−24.

[23] LEI Q, LI Z, ZHU A Y, QIU W T, LIANG S Q. The transformation behavior of Cu−8.0Ni−1.8Si−0.6Sn−0.15Mg alloy during isothermal heat treatment [J]. Materials Characterization, 2011, 62(9): 904−911.

[24] WANG X, XIAO Z, QIU W T, LI Z, LIU F. The evolution of microstructure and properties of a Cu−Ti−Cr−Mg−Si alloy with high strength during the multi-stage thermomechanical treatment [J]. Materials Science and Engineering A, 2021, 803: 140510.

[25] LI J, HUANG G J, MI X J, PENG L J, XIE H F, KANG Y L. Relationship between the microstructure and properties of a peak aged Cu−Ni−Co−Si alloy [J]. Materials Science and Technology, 2019, 35(5): 606−614.

[26] HUANG J Z, XIAO Z, DAI J, LI Z, JIANG H Y, WANG W, ZHANG X X. Microstructure and properties of a novel Cu−Ni−Co−Si−Mg alloy with super-high strength and conductivity [J]. Materials Science and Engineering A, 2019, 744: 754−763.

[27] LI Z, ZHU X, JIANG Y B, QIAN L H, XIE J X. Composition design, phase transition and fabrication of copper alloys with high strength and electrical conductivity [J]. Chin J Nonferrous Met (in Chinese), 2019, 29: 2009−2049.

[28] PAN S B, WANG Y J, YU J X, YANG M J, ZHANG Y Q, WEI H T, CHEN Y C, WU J W, HAN J J, WANG C P, LIU X J. Accelerated discovery of high-performance Cu−Ni−Co−Si alloys through machine learning [J]. Materials & Design, 2021, 209: 109929.

[29] BAN Y J, ZHANG Y, TIAN B H, SONG K X, ZHOU M, ZHANG X H, JIA Y L, LI X, GENG Y F, LIU Y, VOLINSKY A A. EBSD analysis of hot deformation behavior of Cu−Ni−Co−Si−Cr alloy [J]. Materials Characterization, 2020, 169: 110656.

[30] ZHAO Z Q, XIAO Z, LI Z, MA M Z, DAI J. Effect of magnesium on microstructure and properties of Cu−Cr alloy [J]. Journal of Alloys and Compounds, 2018, 752: 191−197.

[31] CHENG J Y, TANG B B, YU F X, SHEN B. Evaluation of nanoscaled precipitates in a Cu−Ni−Si−Cr alloy during aging [J]. Journal of Alloys and Compounds, 2014, 614: 189−195.

[32] WANG M, ZHANG R, XIAO Z, GONG S, JIANG Y B, LI Z. Microstructure and properties of Cu−10wt.%Fe alloy produced by double melt mixed casting and multi-stage thermomechanical treatment [J]. Journal of Alloys and Compounds, 2020, 820: 153323.

[33] YASI J A, HECTOR JR L G, TRINKLE D R. First-principles data for solid-solution strengthening of magnesium: From geometry and chemistry to properties [J]. Acta Materialia, 2010, 58(17): 5704−5713.

[34] SUN X L, JIE J C, WANG P F, QIN B L, MA X D, WANG T M, LI T J. Effects of Co and Si additions and cryogenic rolling on structure and properties of Cu−Cr alloys [J]. Materials Science and Engineering A, 2019, 740/741: 165−173.
[35] MABUCHI M, HIGASHI K. Strengthening mechanisms of Mg−Si alloys [J]. Acta Materialia, 1996, 44(11): 4611−4618.
[36] HE J Y, WANG H, HUANG H L, XU X D, CHEN M W, WU Y, LIU X J, NIEH T G, AN K, LU Z P. A precipitation-hardened high-entropy alloy with outstanding tensile properties [J]. Acta Materialia, 2016, 102: 187−196.
[37] LEI Q, XIAO Z, HU W P, DERBY B, LI Z. Phase transformation behaviors and properties of a high strength Cu−Ni−Si alloy [J]. Materials Science and Engineering A, 2017, 697: 37−47.
[38] CONRAD H, NARAYAN J. On the grain size softening in nanocrystalline materials [J]. Scripta Materialia, 2000, 42(11): 1025−1030.
[39] LI Y S, TAO N R, LU K. Microstructural evolution and nanostructure formation in copper during dynamic plastic deformation at cryogenic temperatures [J]. Acta Materialia, 2008, 56(2): 230−241.
[40] FURUKAWA M, IWAHASHI Y, HORITA Z, NEMOTO M, TSENEV N K, VALIEV R Z, LANGDON T G. Structural evolution and the Hall−Petch relationship in an Al−Mg−Li−Zr alloy with ultra-fine grain size [J]. Acta Materialia, 1997, 45(11): 4751−4757.
[41] WU Z H, GAO Y F, BEI H B. Thermal activation mechanisms and Labusch-type strengthening analysis for a family of high-entropy and equiatomic solid-solution alloys [J]. Acta Materialia, 2016, 120: 108−119.
[42] WEN H M, TOPPING T D, ISHEIM D, SEIDMAN D N, LAVERNIA E J. Strengthening mechanisms in a high-strength bulk nanostructured Cu−Zn−Al alloy processed via cryomilling and spark plasma sintering [J]. Acta Materialia, 2013, 61(8): 2769−2782.
[43] WU Y K, LI Y, LU J Y, TAN S, JIANG F, SUN J. Correlations between microstructures and properties of Cu−Ni−Si−Cr alloy [J]. Materials Science and Engineering A, 2018, 731: 403−412.

# 多级形变热处理 Cu−Ni−Co−Si−Cr−Mg 合金的组织与性能

秦柳馨[1]，周 涛[1]，姜晓羽[1]，王 檬[1]，胡锦辉[1]，吴子潇[1]，孟祥鹏[1]，姜雁斌[1,2]，李 周[1,2]

1. 中南大学 材料科学与工程学院，长沙 410083；
2. 中南大学 粉末冶金国家重点实验室，长沙 410083

**摘 要：**设计并制备一种高强度、中等导电性的 Cu−1.3Ni−1.2Co−0.7Si−0.3Cr−0.1 Mg 合金。研究多级形变热处理对合金组织和性能的影响及其强化机制。结果表明，在时效过程中，高密度位错区和亚晶界处析出大量纳米级的 $\beta$-$Ni_3Si$、$\delta$-$(Ni,Co)_2Si$ 和 Cr 相颗粒，凝固过程中形成亚微米级 $Cr_3Si$ 相。该合金的抗拉强度、屈服强度和电导率分别为 882 MPa、857 MPa 和 46.7% (IACS)。通过强化模型的计算和强度测试，该合金的主要强化机制为析出强化、应变强化和亚结构强化。

**关键词：**多元合金化；显微组织演变；析出相；性能；强化机制

**(Edited by Xiang-qun LI)**